High-Performance 3D Printed Mechanically Interlocked Soft–Hard Interfaces of Hydrogels and Polylactide

Kunkels, L. B.; Saldívar, M. Cruz; Putra, N. E.; Kruize, C. Pitta; Panahkhahi, S.; Leeflang, M. A.; Fratila-Apachitei, L. E.; Zadpoor, A. A.; Mirzaali, M. J.

DOI
10.1002/admt.202401081

Publication date
2025

Document Version
Final published version

Published in
Advanced Materials Technologies

ADVANCED MATERIALS TECHNOLOGIES
www.advmattechnol.de

High-Performance 3D Printed Mechanically Interlocked Soft–Hard Interfaces of Hydrogels and Polylactide

L.B. Kunkels, M. Cruz Saldívar, N.E. Putra, C. Pitta Kruize, S. Panahkhahi, M.A. Leeflang, L.E. Fratila-Apachitei, A.A. Zadpoor, and M.J. Mirzaali**

High-performance soft–hard interfaces are inherently difficult to fabricate due to the dissimilar mechanical properties of both materials, especially when connecting extremely soft biomaterials, such as hydrogels, to much harder biomaterials, such as rigid polymers. Nevertheless, there is significant clinical demand for synthetic soft–hard interfaces. Here, soft–hard interface geometries are proposed, designed with the aid of computational analyses and fabricated as 3D-printed hydrogel-to-polylactide (PLA) structures. Two primary interlocking geometries (i.e., anti-trapezoidal (AT) and double-hook (DH)) are used to study the envelope of 2.5D geometric interlocking designs, fabricated through hybrid 3D printing, combining pneumatic extrusion with fused deposition modeling. Finite-element analysis, uniaxial tensile tests, and digital image correlation (DIC) are used to characterize the geometries and identify parameters that significantly influence their mechanical performance. These findings reveal significant differences between geometric designs, where DH geometries performed significantly better than AT geometries, exhibiting a 190% increase in the maximum force, F_{max}, and a 340% increase in the fracture toughness, W. Compared to the control groups (i.e., flat, inset, and 90° interfaces), F_{max} and W values increased by 500%–990% and 350%–1200%, respectively. The findings of this study can serve as a guideline for the design and fabrication of efficient soft–hard interfaces with performances close to predicted values.

1. Introduction

High-performance soft–hard interfaces are inherently difficult to fabricate as the dissimilarity in the mechanical properties of both materials leads to severe stress concentrations (i.e., localized areas that experience significantly higher stress than the surrounding material)[1] that drastically reduce the mechanical performance of such interfaces, particularly under tension. Furthermore, it is often challenging to connect extremely soft biomaterials, such as hydrogels, and hard biomaterials, such as hard polymers or metals, due to the limited adhesion between both phases and the fact that multiple safety and functional requirements, including high mechanical performance, chemical biocompatibility, and biodegradability, severely limit the available choices of adhesives[2] Despite these challenges, there is a significant demand for synthetic soft–hard interfaces that could be used to treat several conditions where the interface of a soft and a hard tissue is damaged and requires reconstruction either through implants or through regeneration of both tissue types. For example, the replacement of damaged bone-tendon connections requires the development of a robust artificial interface that can endure complex loading conditions.[3–5] A second example is the scaffolds used for the regeneration of cartilage-bone connections, which are needed to treat osteochondral defects.[6,7] Current treatments, however, often lead to reduced efficacy of the interface due to the introduction of new stress concentration regions at the regions of soft–hard interface and compromised mechanical properties.[8] As a result, for example for the case of bone-tendon connections, retear rates of rotator cuff injuries, even after surgical intervention, range from 20–94%.[8,9] Similarly, osteochondral defects including those caused by osteoarthritis impact over 500 million people worldwide, while current treatments do not fully restore cartilage function and the affected subchondral bone, resulting in the need for additional surgeries, such as total joint arthroplasty or joint fusion.[10] In the case of bone tumor resections, large implants are often used for the reconstruction of the resulting defect and the provision of a muscle-reattachment site. Although this method has shown

L. Kunkels, M. C. Saldívar, N. Putra, C. P. Kruize, S. Panahkhahi, M. Leeflang, L. Fratila-Apachitei, A. Zadpoor, M. Mirzaali
Department of Biomechanical Engineering
Faculty of Mechanical Engineering
Delft University of Technology (TU Delft)
Mekelweg 2, Delft 2628 CD, The Netherlands
E-mail: L.B.Kunkels@tudelft.nl; M.J.Mirzaali@tudelft.nl

S. Panahkhahi
Research Group Technology for Healthcare
Centre of Expertise Health Innovation
The Hague University of Applied Science
Delft 2628 AL, The Netherlands

The ORCID identification number(s) for the author(s) of this article can be found under https://doi.org/10.1002/admt.202401081

DOI: 10.1002/admt.202401081

potential for soft–hard tissue reattachment and enhanced osseointegration, the realized clinical outcomes often failed to fully meet expectations.[11]

Recently, significant progress has been made in the field of artificial soft–hard interface fabrication with the aim of replicating natural tissues and offering solutions for their repair or replacement when damaged.[12,13] A widely used technique involves the use of chemical adhesives or coatings to bind two disparate components.[14] A different method employs functional gradients formed by material composites where a gradual material transition effectively mitigates potential stress concentrations that arise across the transition between different materials.[15–17] Finally, it is possible to use geometrical design to address this challenge, establishing purely mechanical connections through (complex) interlocking shapes.[18] Despite the diversity of these methodologies, most solutions are rendered either wholly or partially ineffective in the fabrication of extremely soft–hard interfaces where the mechanical property disparity spans several orders of magnitude, making it challenging to replicate the hierarchical structure of natural interfaces.[19,20] Although each technique offers specific benefits, they also have critical limitations in one or more aspects of successful interface engineering, including biocompatibility, fabrication complexity, and material composition.[4]

The intrinsic disparity in mechanical properties between the extremely soft and hard materials makes the seamless integration of extreme soft–hard interfaces inherently difficult, leading to complications at the interface.[1] These complications encompass a range of issues, including discrepancies in load-bearing capacities, imperfections in geometrical material binding,[1] and the emergence of stress concentrations due to abrupt transitions at the interface.[21–23] In contrast to artificial soft–hard interfaces, natural interfaces exhibit exceptional binding characteristics and a high level of structural and functional adhesion between soft and hard materials.[24] Nature accomplishes this through gradual variation in the chemical compositional and intricate geometrical designs that facilitate the formation of mechanically interlocked interfaces.[25] A notable example of such interfaces is the tendon enthesis which connects the hard bony tissue (≈20 GPa)[26] to the soft tendonous tissue with an elastic stiffness that is 2–3 orders of magnitude lower.[19] This natural interface, spanning a relatively short distance (<1 mm), is characterized by morphological interdigitations and exhibits exceptional interfacial strength, toughness, and damage tolerance.[19] Damage tolerance is of critical importance in biological applications to ensure that the hard and soft phases remain connected following initial failure, thus permitting the regeneration of the interface.[27] Moreover, stress concentrations and imperfect interfacing are of high significance in mitigating stress-induced failures as proven by the developments in architected material design and interlocking geometries.[28] Therefore, taking inspiration from nature, both in terms of geometric and chemical interface designs, serves as a promising pathway toward the development of high-performance biomimetic soft–hard interfaces.

To ensure the successful engineering of such interfaces and their effective clinical application, it is imperative for the interface materials to exhibit biocompatibility. Biocompatibility is essential to prevent cytotoxicity in the human body, to enable structural integration of the implant into surrounding native tissues, and to fulfill the required functionalities. For the hard phase, this translates to the use of non-cytotoxic materials. For the soft phase, however, an additional requirement is the ability to provide a biomimetic environment for the proliferation of mammalian cells. Hydrogels could be highly effective in this regard. Hydrogels are biphasic gel-like materials that are primarily composed of water confined within a hydrophilic polymer network, providing the material with structural integrity that resembles extracellular matrix (ECM) of soft tissues.[29] These characteristics create an excellent environment for the survival and proliferation of cells while the versatile nature of hydrogel facilitates their processing for (bio)printing. This in turn allows for the design of structures with mechanical properties resembling those found in soft tissues.[29,30] The (bio)printing of hydrogels paves the way for the development of complex soft phases that closely mimic those found in nature, highlighting the need to apply advanced techniques for fabricating extremely soft–hard interfaces.

The fabrication of multi-phasic scaffolds composed of materials ranging from extremely soft to extremely hard introduces increased complexity to their fabrication process.[31] The biocompatibility requirements, particularly in terms of mitigating stress concentrations and ensuring proper material binding, necessitates a versatile and highly controllable fabrication method capable of processing different types of biomaterials.[31] It is these requirements that render aforementioned fabrication solutions inadequate for replicating similar tissue interfaces, as the applicability of hydrogel has not been tested. Additionally, conventional techniques fall short in realizing intricate interfacial geometries and the requisite control over such multi-material distribution.[20] Consequently, the utilization of versatile advanced manufacturing techniques become imperative to produce such intricate interlocking designs. The emergence of additive manufacturing (AM, = 3D printing) techniques, particularly their ability to precisely create both hard and soft materials, has addressed these manufacturing limitations and has paved the way for the fabrication of biomimetic soft–hard interfaces.[4,20,31,32] By utilizing the strengths of 3D printing, this technology can advance the field of personalized medicine by enabling the fabrication of patient-specific interface implant designs tailored to meet individual anatomical and biomechanical needs. This personalized approach has the potential to improve clinical outcomes by ensuring that interface implants fit the specific requirements of each patient, reducing the likelihood of complications and enhancing long-term stability.

In this study, we investigate the design envelope of simple 2.5D geometric designs and their efficacy in mechanically interlocking hydrogels with hard phases. Chemical bonding was deliberately not used in this study to focus exclusively on the mechanical interlocking capabilities of the geometric designs. Specifically, we examine two distinct interlocking designs, namely antitrapezoidal (AT) and double-hook (DH) systems (**Figure 1**). These designs are chosen for their inherently high interfacial strengths, respectable levels of damage tolerances, and tight interlocking properties.[27,33] To facilitate the controlled design of soft–hard interfaces, these geometries are parametrized and examined through computational models. The insights gained from

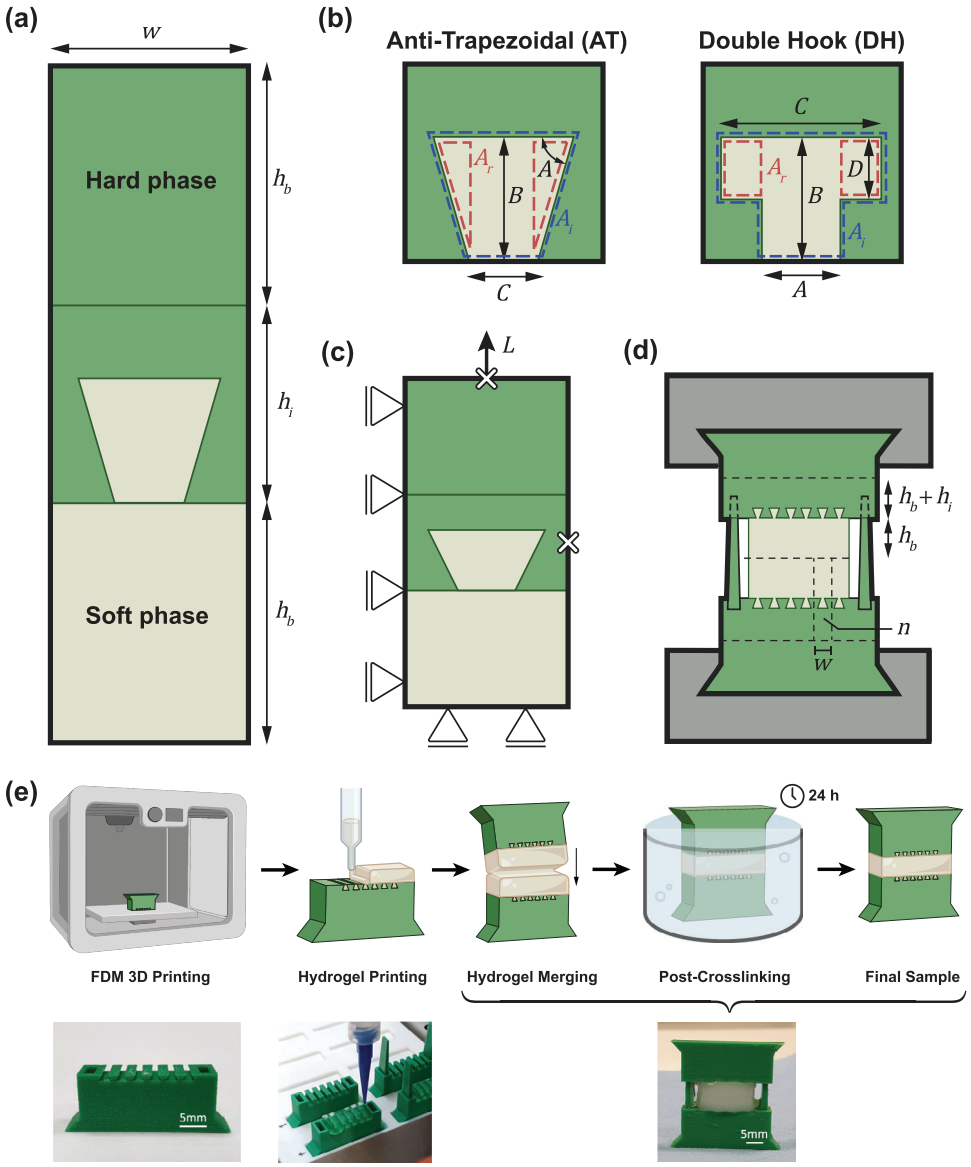

Figure 1. Schematic representation of the soft–hard interface design. a) A single unit cell consisting of three sections: a hard-, soft-, and interface part. b) Design parameters of the two interface geometries. c) Boundary conditions for the simulation model. Symmetry conditions constrain the left- and bottom edges of the model, while the right- and top edges are tied to respective reference points (marked ×). A tensile load is applied longitudinally to the top reference point. d) Tensile test configuration. The interface consists of multiple (*n*) unit cells in parallel. e) Fabrication process of the soft–hard specimens used in this study.

these simulations are then used to design and realize several hydrogel-plastic soft–hard interfaces. These interfaces are fabricated through a hybrid 3D printing technique that combines extrusion-based printing of the soft-phase biomaterials, such as hydrogel, with fused deposition modeling (FDM) to print the hard phase (e.g., hard polymers). The fabricated specimens undergo tensile testing to evaluate their mechanical characteristics, after which a comparison between the experimental and simulated mechanical properties is conducted to assess and benchmark their mechanical performance. Ultimately, this research will establish a baseline for the design and fabrication of soft–hard interfaces with potential applications in both implantable medical devices and regenerative medicine.

2. Results and Discussion

2.1. Design Considerations for Mechanically Interlocked Interfaces

2.1.1. Computational Models

The computational results revealed significant variations in the performance of different interface variants for both AT and DH type geometries. The range of maximum force (F_{max}) was highly dependent on the design type (**Figure 2a**). For the AT designs, F_{max} varied between 3.4×10^{-3} and 1.5 N, while it ranged between 5.6×10^{-2} and 1.0 N for the DH designs. The maximum

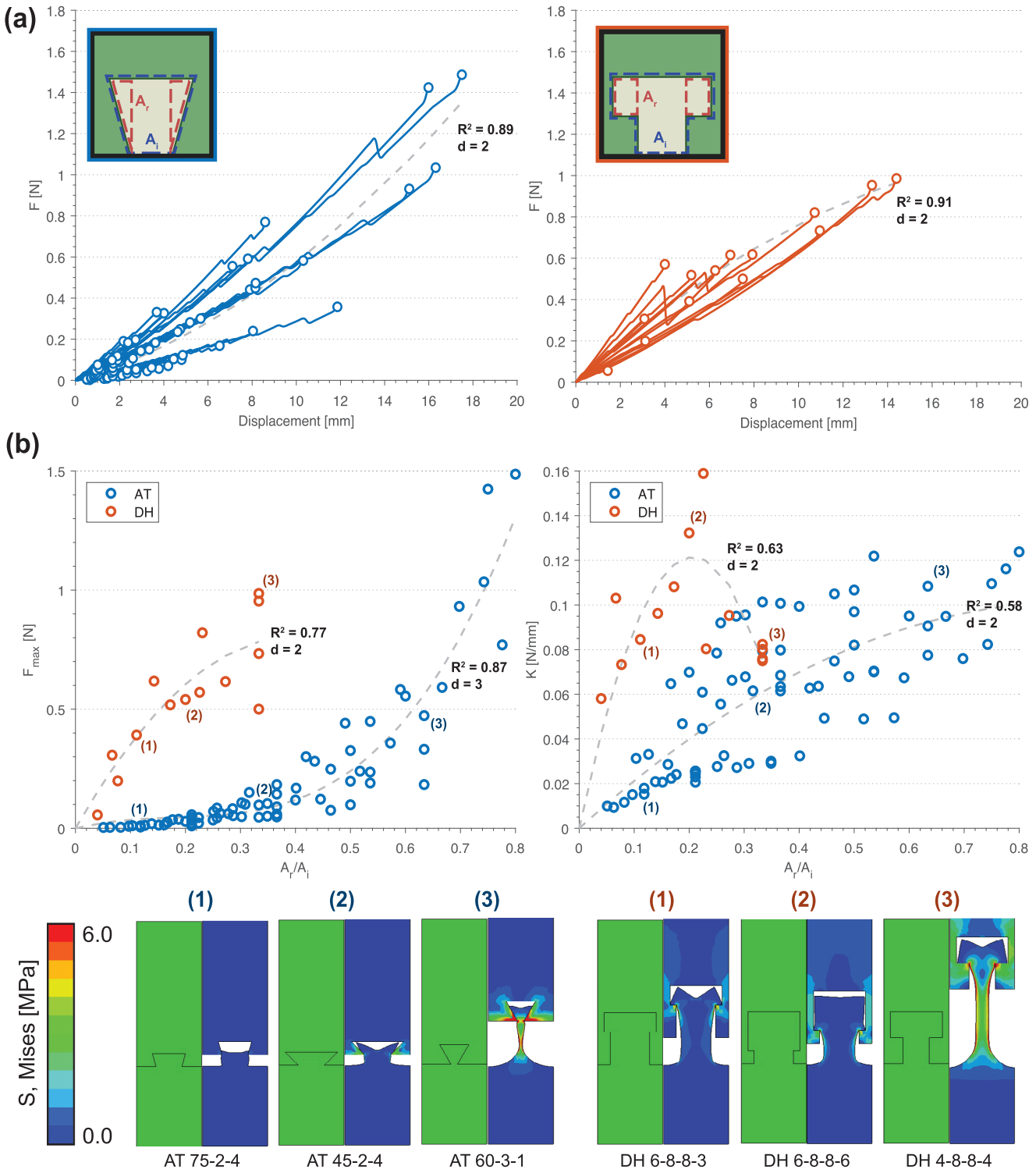

Figure 2. FE results of all interface variations for each geometry. Maximum force values are marked with a circle at the end of each curve. a) Force–displacement curves for all AT (left) and DH (right) variations. A trend line, shown as a polynomial fit with degree d and R^2, suggests a slight exponential trend. Overall, DH designs demonstrate higher peak forces than AT designs, with more DH variations reaching greater maximum force values. b) Linear regression of maximum force (F_{max}) and stiffness (K) as a function of the A_r:A_i ratio. A selection of designs with varying A_r:A_i ratios are displayed at 80% of the total applied strain, illustrating the distribution of stress concentrations under tensile loading conditions. Higher A_r:A_i ratios show significantly larger deformations than the lower ratios.

value of the AT designs was 1.5 times higher than that of the DH designs. This data shows that the DH designs varied much less than the AT designs, where the variance of the DH designs is only 4% of that of AT designs. The maximum displacements ranged between 0.5 and 1.7×10^1 mm for the AT designs and between 1.4 and 1.4×10^1 mm for the DH designs, where the maximum value of the AT designs was 82% of the maximum value of the DH designs. Once more, the DH designs showed a much smaller variation, namely 30% of that of AT. A key observation from these results is the much larger variation in the interface performance of the AT designs as compared to the DH designs both for F_{max} (95% lower for DH designs) and maximum displacements (70% lower for DH designs), with most DH designs exhibiting an F_{max} of 0.59 ± 0.29 N. The force-displacement plots generally exhibited nonlinear characteristics, tending toward an exponential trend, described using a second-degree polynomial through linear regression with a coefficient of determination (R^2) of 0.89 for the AT models and 0.91 for DH models. Notably, abrupt drops in F can be observed along these plots. This phenomenon is attributed to the behavior of the elements used in our computational model. As the total displacement increases, the elements suddenly "slip" past the resisting edge of the interface, resulting in the observed sudden reductions in the reaction force.

To mitigate the impact of such (computational) artifacts (i.e., mesh element "slip") observed in the force-displacement plots, we examined F_{max} in relation to the A_r:A_i ratio for each design. Additionally, to provide deeper insight, we analyzed the stress concentrations at F_{max} for three representative designs from each geometry type (Figure 2b-bottom row). Notably, the data revealed distinct trends that could be described using a second-degree polynomial, as evidenced by linear regressions with a coefficient of determination (R^2) of 0.87 for the AT models and 0.77 for the DH models, respectively. In general, the trends indicated that higher A_r:A_i ratios resulted in increased F_{max} values. This observation aligns with the mechanical behavior of interfaces, as lower ratios result in less tightly confined interfaces, exerting weaker resistance forces against the soft phase. Conversely, higher ratios lead to tighter confinements and, thus, greater forces are required to displace the soft phase through the interface opening. For an A_r:A_i ratio of 1, the geometry would form a closed interface, disjoining the soft material interface from the bulk, while a ratio of 0 would denote a nonfunctional interface due to the absence of a resisting edge. Additionally, designs with higher A_r:A_i ratios (i.e., 0.6 for the AT models and 0.3 for the DH models) exhibited unrealistically large strains in the soft phases, suggesting the likelihood of hydrogel rupture in real-world scenarios. Consequently, the computational model is most reliable below these thresholds.

In the AT group, most designs had an A_r:A_i ratio between 0 and 0.4, each with an F_{max} value below 0.2 N (Figure 2b). The DH designs demonstrated a greater variability in both the A_r:A_i ratios and F_{max}, indicating a higher potential for rational design within the context of the DH geometry (e.g., in terms of the A_r:A_i ratio) as opposed to the AT geometry, which offers limited combinations of parameters *A*, *B*, *C* that yield higher ratios and, thus, higher values of F_{max}. However, optimally designed AT geometries could potentially achieve higher F_{max} values than the DH geometries, as suggested by the observed trends.

To further elucidate the mechanical characteristics of the interfaces, we also examined the stiffness trends of the interfaces (Figure 2b). For the DH designs, the stiffness trend appeared to align with the F_{max} trend. For the AT designs, however, we observed a more nonlinear trend. Notably, both trends were characterized by second-degree polynomials with lower R^2 values than for the F_{max} fits, at 0.63 for DH and 0.58 for the AT designs. A possible explanation for this disparity is that stiffness, unlike maximum force, may not be as strongly influenced by the A_r:A_i ratio alone, indicating that other factors might also play a role in determining the stiffness characteristics. Interestingly, for the DH designs, a pronounced decrease in F_{max} was observed for A_r:A_i ratios exceeding 0.22 which coincided with a larger variation in F_{max}. This might indicate a lower simulation accuracy than at lower ratios. In contrast, the AT designs showed a consistent trend where higher A_r:A_i ratios were associated with increased stiffness, similar to the F_{max} trend.

2.1.2. Experimental Observations

The four 3D printed interface designs demonstrated tightly interlocked infills with no visible air gaps at the corners of the interface or air bubbles within the soft phase. The tensile tests of these specimens yielded distinct force-displacement curves, displayed alongside their mean values, standard deviations, and F_{max} (**Figure 3a**). Additionally, images showcasing specimens at different stages – elastic, failure point, and post-failure – are provided for visual reference (Figure 3a). A notable observation across all the interfaces is a similar failure point, ≈0.8 mm displacement. However, variations in F_{max} were evident (ranging between 5.9×10^{-1} and 1.1 N) with the DH designs generally exhibiting higher F_{max} values as compared to the AT designs. Additionally, the results highlight a clear difference in the characteristic behavior between the AT and DH designs, where the AT designs tended to fail more abruptly, whereas the DH designs displayed a more gradual failure, suggesting higher fracture toughness values. This difference is visually discernible in the images of the specimens, where the AT interfaces show simultaneous failure across all the unit cells, while the DH interfaces demonstrate a progressive, zipper-like failure starting from one unit cell and extending to the adjacent ones. This difference could be attributed to the contrasting resistive geometries of both designs. In the DH designs, the resistive edges are oriented perpendicularly to the tensile direction, offering more resistance, whereas the sloped resistive edges of the AT designs facilitate an easier detachment of the soft phase from the interface cavity. All failures occurred within the soft phase, either as detachment or slight ruptures at the outer unit cells in the DH designs. In contrast, the hard phase remained intact in all the tests. The standard deviation across the tests indicated consistent behaviors in the elastic region among the replicates of each design (e.g., forces of 0.3 ± 0.05, 0.3 ± 0.07, 0.4 ± 0.06, and 0.6 ± 0.04 N at 0.35 mm displacement for AT 45-3-3, AT 60-4-3, DH 6-8-8-7 and DH 4-8-6-6, respectively). Greater variability was observed in the failure region and the actual F_{max} (e.g., forces of 0.2 ± 0.2, 0.5 ± 0.1, 0.6 ± 0.2, and 1.1 ± 0.2 N at 1.3 mm displacement for AT 45-3-3, AT 60-4-3, DH 6-8-8-7 and DH 4-8-6-6, respectively). Despite this variance, consistent general failure behaviors were observed among the specimens belonging to the same design, underscoring the reproducibility of the force-displacement

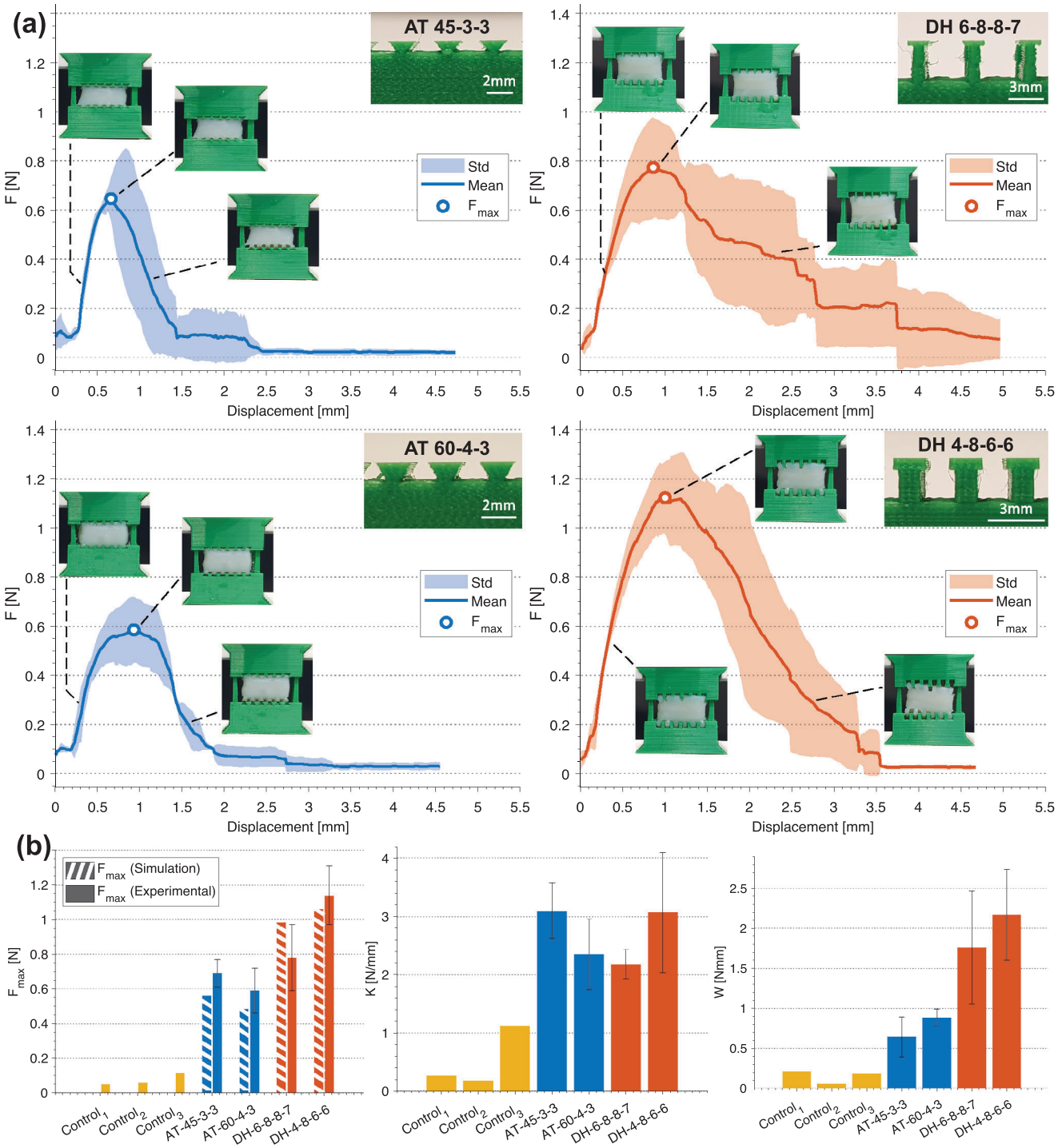

Figure 3. Tensile-test results for the four interface designs. a) Force–displacement curves of each of the four interfaces. b) Comparison of ultimate tensile strength (F_{max}), stiffness (K), and toughness (W) including control groups. F_{max} is compared against the (scaled) simulation results ($^{*}p < 0.05$, $^{**}p < 0.01$, $n = 3$).

behaviors corresponding to each combination of design parameters. Variations in the force-displacement magnitudes may have been caused by several factors, such as minor differences in the hydrogel crosslinking or printing process, including printing imperfections. During the hydrogel printing stage, a variation in the pressure of ±5 kPa (≈10% of the total pressure) was observed, suggesting that the observed standard deviations primarily stem from variations in the hydrogel material at the ink-formulation stage. The relatively minor degree of variation observed in our experiments supports the reproducibility of the presented

results and highlights the appropriateness of the applied methods.

2.2. Role of Geometrical Design

We compared our computational results with the experimental data to evaluate the validity of our computational models. We used Equation (1) (see the Materials and Methods section below) to scale the computationally derived values of F_{max}, thereby making sure they correspond to the dimensions of the tensile test specimens used in our experiments and facilitating a direct comparison between both result types (Figure 3b). No significant differences were observed between the simulated and experimental results (p values of 0.49, 0.56, 0.28, and 0.65 for AT 45-3-3, AT 60-4-3, DH 6-8-8-7 and DH 4-8-6-6, respectively). Both computationally and experimentally obtained values of F_{max} suggested a similar trend regarding the performance of different interface designs.

In an extended analysis of the tensile test data, we compared F_{max}, K, and W for each of the four interface designs (Figure 3b). This data revealed a relatively consistent stiffness, K, across all the interfaces (mean values ranging between 2.2 and 3.1 N mm^{-1}) with only minor, non-significant differences ($p > 0.1$). This observation aligns with our expectation that the system stiffness would predominately be determined by the soft phase, due to an excessive difference (factor 10^6) between the elastic moduli of both phases. In natural interfaces (e.g., tendon-to-bone insertion sites), the interface is actually observed to exhibit a lower stiffness than the neighboring materials, which is postulated to aid in the reduction of soft-to-hard stress concentrations.[23] The similar values of K observed across all the interface designs corroborates the validity of the specimen designs, as the similar values of stiffness across all interface designs indicates the stiffness is determined primarily by the soft bulk (which is kept constant across all interfaces) and not by the interface design. Similarly to how the soft phase dominates the characteristic stiffness of the system, the interface largely determines F_{max} and the failure behavior of the system, and consequently its toughness, W. A comparative analysis of W reflects this, as substantial differences between the AT and DH designs and their variations were observed, in line with the patterns exhibited by the force–displacement curves depicted in Figure 3a. The W values range between 0.6 and 2.2 N·mm, where the DH designs demonstrating superior performance over the AT designs, with significant differences between AT 45-3-3 and DH 6-8-8-7 ($p = 0.02$), AT 45-3-3 and DH 4-8-6-6 ($p = 0.004$) and AT 60-4-3 and DH 4-8-6-6 ($p = 0.01$). A comparative analysis of F_{max} shows a similar difference between the performance of the AT and DH designs, with significant differences between DH 4-8-6-6 and AT 45-3-3 ($p = 0.005$), AT 60-4-3 ($p = 0.002$) and DH 6-8-8-7 ($p = 0.02$). Specifically, there was a difference of 190% and 340% between the maximum and minimum values of in F_{max} and W, respectively. However, the DH designs also exhibited much larger standard deviations of W (0.71 and 0.57 N·mm) as compared to AT designs (0.25 and 0.11 N·mm), likely as a result of their different failure mechanics. Despite this, the large values of F_{max} paired with the similarly large values of W suggest that the DH designs possess promising interface characteristics.

To put the performance of our interface designs in perspective, we compared them with control specimens (Figure 3b). Recognizing that certain characteristics inherent to the 3D printing process (e.g., ribbed surfaces due to layer squish and plastic stringing due to nozzle oozing) potentially increase adhesion between the phases by enlarging the contact area, creating small resisting edges, and increasing frictional contact. For this reason, three different control groups were designed to evaluate the influence of these characteristics (see Figure S1, Supporting Information). The first control group (control 1) consisted of a flat interface with no specific geometry. The second (control 2) featured a flat control with an inset, designed to mimic the rougher surface characteristic of the actual interface surface. The third (control 3) presented a DH geometry without a resisting edge, effectively forming a 90° interface. In the case of control 2, complete failure was observed almost immediately upon applying tensile displacement. The measured F_{max} of 0.06 N with a measurement accuracy of ± 0.025 N and a K of 0.18 N mm^{-1} suggests negligible stress-worthiness. Control 1 exhibited partial failure during the post-crosslinking stage, indicating inherent instability even before testing. Control 3 did withstand slightly higher tensile forces than the other control groups (F_{max} of 0.1 N), indicating that the inaccuracies caused by the 3D printing process (Figure S1b, Supporting Information) did contribute to a minor interlocking effect. Together with a measured K of 1.1 N mm^{-1}, control 3 exhibited higher values of F_{max} and K as compared to control 2 (0.06 N and 0.9 N mm^{-1} higher, respectively), its low toughness W (0.18 N·mm) suggests that these printing-induced effects were relatively insignificant as compared to the influence of interlocking mechanisms studied here. When juxtaposed with the control groups, the four interface designs demonstrated a remarkable improvement in performance: F_{max} values exceeded those of the controls by over 500%, while W values were greater by more than 350%. For the most effective interface, DH 4-8-6-6, this increase was even more pronounced, with F_{max} and W exceeding control 3 by 990% and 1200%, respectively. These findings underscore the significant effects of interlocking mechanisms in general and their geometrical design in particular on the mechanical performance of artificially fabricated extremely soft–hard interfaces.

2.3. Comparison Between Different Printing Technologies

To examine the strain-distribution patterns of the tensile specimens, Polyjet-printed specimens were produced to allow for DIC testing using a painted black-and-white speckle pattern. The DIC results (**Figure 4a**) revealed that strain in each interface design manifested predominantly in the soft phase, especially concentrated along and at the corners of the resisting edges of the hard phase. This pattern aligns with intuitive expectations, as these regions are the most susceptible to the contact forces exerted by the resisting edges. A comparative analysis of the strain distributions between the simulations and DIC images (Figure 4b) showed a strong similarity between the experimentally and numerically obtained strain distributions, particularly within the regions exhibiting strain concentrations. Geometry-specific strain-distribution patterns were evident in both the simulations and experiments: the AT geometries exhibited concentrated strain regions initially in the soft phase at the corners of the resisting

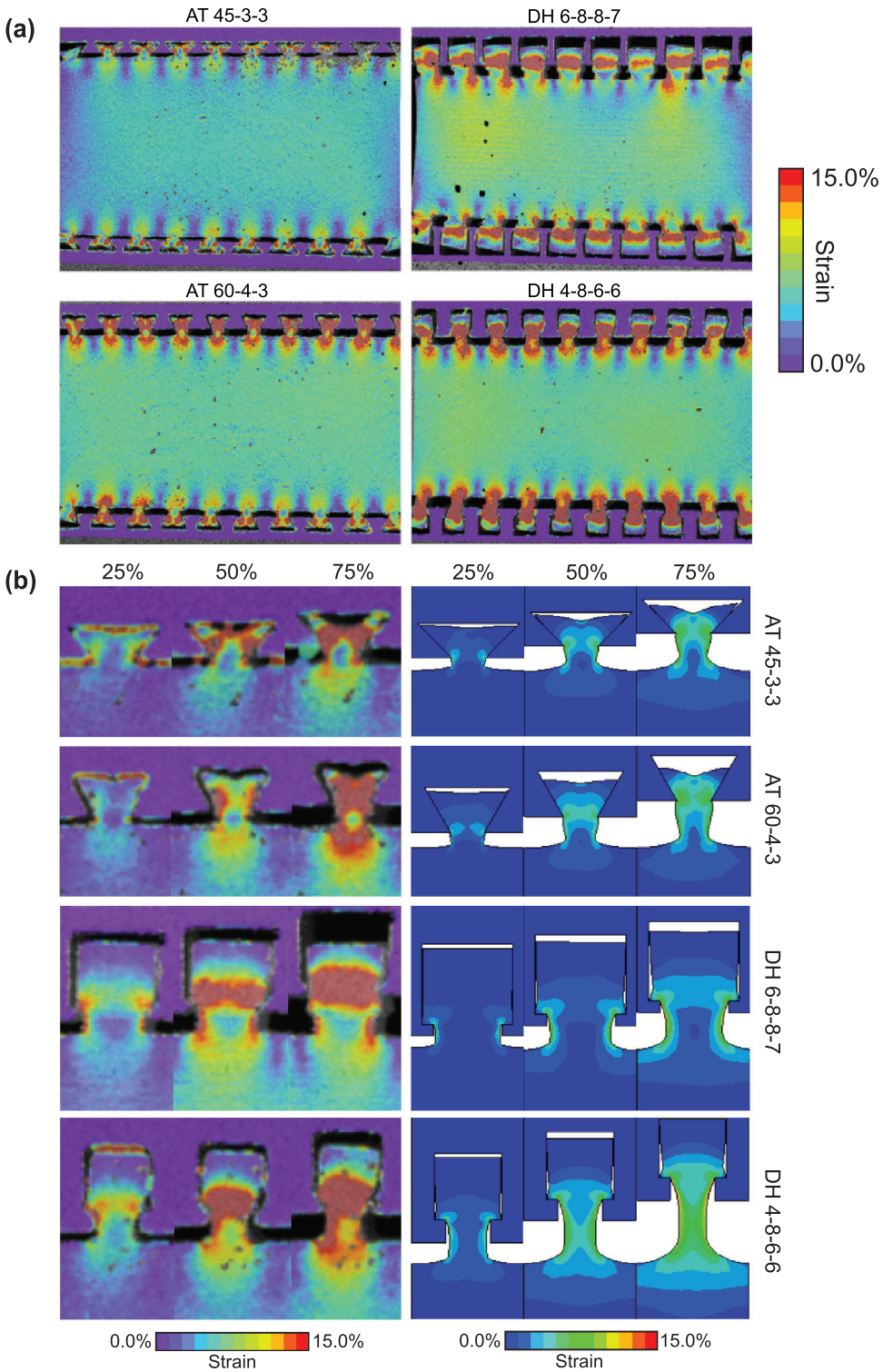

Figure 4. Digital Image Correlation (DIC) of Polyjet-printed four interface designs. a) Full-specimen image, at 75% of total applied strain. b) Comparison of strain-progression of a single interface cell between experimental (left) and simulated (right) models, shown at 25%, 50%, and 75% of total applied strain.

edge, whereas the DH geometries showed strain extending along the parallel edge. For both geometries, the strain-concentration regions then extend horizontally toward each other, while forming a lower intensity directly below the resisting edge within the center of the neck. Besides these strong similarities, slight disparities between the simulations and experiments were found as well. For instance, at 75% total applied strain, the simulation of DH 4-8-6-6 showed the strains mostly concentrated in the neck, while in the experiments, the strains were mostly concentrated in the head. This discrepancy suggests that the simulated material may exhibit higher compliance as compared to the actual material. Such findings show that while computational models can generally predict physical material behavior, experimental validation remains crucial for accurately designing soft–hard interfaces. Overall, our results indicate that the computational models employed in this study provide a reliable approximation of the mechanical behavior of the interfaces.

While the current methodology facilitates the predictive design of soft–hard interfaces, it is important to acknowledge certain limitations. Although uniaxial tensile tests provide clear insights into the mechanical performance of these soft–hard interfaces under simple uniaxial loading conditions, real-world applications particularly in biomedical devices, often involve more complex loading environments, such as multiaxial loading, cyclic stresses, and varying strain rates. These factors could significantly influence the performance and mechanical behavior of the interfaces and may result in different failure modes or altered mechanical responses as compared to those observed in uniaxial tests.

Moreover, the presented computational model represents an idealized version of the physical system. Although the hydrogel material is modeled as a hyper-elastic material, its (apparent) mechanical properties are likely to vary over time due to various factors such as stress relaxation, creep, hydration, and polymer degradation and damage, particularly under prolonged loading conditions. These time-dependent behaviors were not included in the present model, which may impact its predictive accuracy under more complex loading scenarios. Additionally, while we conducted a mesh sensitivity analysis to ensure the stability and convergence of the results, discrepancies between the model and real-life performance could arise from variations in material properties or geometric imperfections that are difficult to fully capture computationally. Future work could focus on refining the computational model by incorporating time-dependent and nonlinear material behaviors, such as viscoelasticity for the hydrogel phase, to better simulate real-world performance. Sensitivity analyses for material properties and loading conditions could also help identify key parameters that influence the accuracy of the model. Such enhancements would strengthen the predictive framework for designing soft–hard interfaces with improved reliability in complex, application-specific environments.

For clinical applications, the material biocompatibility for specific applications involving soft–hard interfaces is critical. Hydrogels and other soft materials integrated into these interfaces must maintain their mechanical properties and structural integrity in the biological environment, where factors such as hydration, enzymatic degradation, and inflammatory responses can impact material performance. Therefore, future work should focus on specific biomedical applications and should include in vitro and in vivo testing of the materials selected to assess their chemical, mechanical and cellular biocompatibility under relevant clinical conditions, or include the use of 3D bioprinting techniques through the use of cell-loaded hydrogels.

Looking ahead, we advocate for future research exploring the use of varied materials combinations in mechanically interlocked interfaces. Investigating hard and soft phases, such as metals and alternative hydrogels, could provide deeper insights into the versatility and applicability of these interfaces. Additionally, studies focusing on how these interfaces behave under more complex environmental conditions (e.g., testing strain-rate dependence, shear stress conditions, or within an aqueous environment to simulate biological conditions), would be valuable for broadening their potential applications. In the field of 3D printed mechanically interlocked plastic-hydrogel interfaces, this study lays down a foundational framework for the controlled fabrication of high-performance artificial interfaces.

3. Conclusion

We studied how geometrical design and additive manufacturing can be used to create high-performance mechanically interlocked soft–hard interfaces. We fabricated 3D-printed hydrogel-to-polylactide (PLA) structures and analyzed the effects of multiple design parameters on their performance with the aid of computational models. We also developed a parametrized computational model and demonstrated it to be an effective and reliable tool for predicting the ultimate tensile strength of various interface designs. These designs were then reliably replicated using our hybrid extrusion and FDM-based printing technologies. Our findings revealed notable distinctions in the mechanical performance between different geometric designs and their variants. Notably, DH geometries demonstrated a significant enhancement in mechanical properties as compared to AT geometries, exhibiting a 190% increase in the maximum force and a 340% increase in the fracture toughness. As compared to the control groups, the performances of the four interface designs were remarkably higher: F_{max} values exceeded those of the controls by over 500%, while W values were greater by more than 350%. The most effective interface design even showed F_{max} and W exceeding the control groups by at least 990% and 1200%, respectively. Finally, DIC measurements performed on Polyjet-printed specimens showed strong similarities between the experimentally and numerically obtained strain distributions, especially in the regions exhibiting strain concentrations. Our analyses and the data presented here indicate that the performance of mechanically interlocked soft–hard interfaces can be effectively modulated through rational design of the interface geometry. Moreover, the results demonstrate that such performance can be accurately predicted using our computational models, especially when employing realistic interface parameter combinations with respect to the A_r:A_i ratio. This methodology, validated through our study, could serve as a guideline for the design and fabrication of efficient and successful soft–hard interfaces.

Our findings in this study not only contribute to the understanding of interface mechanics but also open novel avenues for practical implementations in areas requiring robust and reliable soft–hard material integration. Furthermore, these results directly contribute to the progress in biomaterial fabrication, medical devices, and tissue engineering. The potential applications

of these findings are vast, offering promising avenues for future innovations in biomaterials and their integration into medical devices.

4. Experimental Section

Computational modeling in the form of finite element analysis (FEA) was employed to parameterize different design features and evaluate them in terms of their maximum force (F_{max}) and stiffness (K). Utilizing insights gained from these simulations, four distinct interfaces were designed with respect to their expected performance. These prototypes were then fabricated using hybrid combination of extrusion and FDM-based 3D printing techniques. The performance of these interfaces was then assessed to validate the results obtained from the simulations. Furthermore, the four interfaces underwent comparative analyses, focusing on the key metrics F_{max}, K, and toughness (W). This comparative approach was instrumental in understanding the relative performance of various interface designs.

Computational Modeling: First, the soft–hard interface was modeled using unit cells comprising three distinct segments: a bulk hard-, a bulk soft-, and an interface section (Figure 1a). To ensure comparability across different geometries, the overall dimensions of the soft–hard models were standardized using a constant bulk height (h_b) for the soft- and hard bulks, while the interface was kept at a constant interface height (h_i). All the sections shared a uniform width (w). Additional hard bulk was incorporated into the interface section, which varied in accordance with the changes in the interface geometry to maintain a constant volume of the soft phase. This approach was chosen to maintain a constant volume of the soft phase, which was assumed to be the predominant driving factor influencing the system stiffness. The impact of geometric design on the tensile properties of mechanically interlocked interfaces was investigated through the parameterizations of two distinct designs of interlocking geometries, namely AT and DH (Figure 1b). The AT model was defined by three independent variables: the trapezoidal angle (A), trapezoidal depth (B), and opening width (C). The DH model was characterized by four independent variables: the opening width (A), total depth (B), hook width (C), and hook thickness (D). Variations of these geometries were created by altering the values of these parameters. Each variation was named according to its geometry type, followed by the assigned parameter values (i.e., "AT *A-B-C*" for AT designs and "DH *A-B-C-D*" for DH designs). For the AT designs, a constraint of $A < 90°$ was applied to ensure the presence of a resistive edge. Similarly, for the DH designs, the constraints of $C > A$ and $B > D$ were applied. By manipulating these parameters, we could alter the ratio between the resisting area (A_r) and total interface area (A_i), which was anticipated to significantly affect the performance of the soft–hard interfaces.

A parametric study was conducted using computational modeling to simulate the tensile behavior of these variations of the geometries. The simulations were performed using Abaqus/CAE 2022 v.6.25 (SIMULIA, Dassault Systèmes, France), using a nonlinear model with hyperelastic constitutive equations. The resulting data were processed with MATLAB R2018b (MathWorks, United States). The computational models were designed to include the same three parts of the unit cell in series: a soft, a hard, and an interface part, the latter containing the target interface geometry (Figure 1c). These models were integrated using a script written in Python v.3.11 (Python Software Foundation, United States). A bulk height of $h_b = 12.2$ mm, an interface height of $h_i = 10$ mm, and a width of $w = 10$ mm were used. Using these parameters, the total unit cell and the soft phase volumes were kept constant while the volume of the hard phase varied with changes in the interface depth (B). To investigate the impact of the geometric parameters on the force–displacement behavior of the interlocking system, simulations of each model were performed using different combinations of the geometrical parameters. For the AT model, A ranged between 30° and 75° in 15° increments. B and C were varied independently from 1 to 5 mm in 1 mm increments. Similar variations were used for the DH model, focusing solely on the relative size of the hook, the A:C ratio, and the B:D ratio, due to the extensive combination of possibilities presented by these four independent variables. This led to a total of 71 models for the AT geometry and 17 models for the DH geometry.

For both the experimental and computational analyses, two distinct materials were selected to represent the hard- and soft phases. The hard phase was made from Tough PLA (Makerpoint, Netherlands), which was characterized by an elastic modulus (E) of 2.3 GPa, a Poisson's ratio (ν) of 0.35,[34] and a density (ρ) of 1.22 g cm^{-3}. This material was modeled as a linear elastic material in the simulations. The soft phase was made from a hydrogel, specifically a 5% (w/v) Sodium Alginate solution (Fisher Scientific, Belgium) in 0.9% NaCl. This hydrogel was modeled as a hyperelastic material using the Ogden strain energy potential, with the following parameters: $\mu = 4.5\times10^{-2}$, $\alpha = 3.61281242$, and $D = 0$, $N = 1$. These parameters were determined using Abaqus from standard tensile test results of a cast hydrogel in a standard shape (ASTM D412-16[35]). For more details, see Note S1 (Supporting Information).

The computational model was optimized with regard to the expected large displacements of the soft phase. Large displacements might cause nonlinear geometric effects (i.e., large deflections or "snap through"), which were accounted for using a default nonlinearity tolerance of 0.05. In addition, the meshing strategy was carefully designed to ensure accurate simulation results, using plane strain elements with a plane strain thickness of 1.0 mm. These elements were 4-node bilinear with reduced integration and hourglass control (CPE4R), to accurately measure material warping. To optimize the mesh for both accuracy and computational efficiency, the selection of the mesh size was informed by a mesh sensitivity analysis (see Note S2, Supporting Information). This analysis led to the use of a global seed size of 1.4 mm. However, to capture the intricacies at the interface more accurately, the local seed sizes at the interface of the soft and hard phases were decreased, resulting in a local seed size of 0.6 mm in the hard phase and 0.1 mm in the soft phase. These local seeds were generated on the interface edges and up to 1.5 mm away from it.

The boundary conditions applied to the computational model directed the displacement exclusively along the tensile load (L) axis. Symmetric boundary conditions were enforced at the bottom ($U_y = R_x = R_z = 0$) and the left ($U_x = R_y = R_z = 0$) edges of the models. Additionally, tie constraints were used to connect all the nodes on the right and top edges to their respective reference points (marked × in Figure 1c), with the right and top edges, respectively, satisfying the conditions $U_y = R_z = 0$ and $U_x = R_z = 0$. Periodic boundary conditions were not employed in our simulations. This decision was based on preliminary comparisons which indicated no significant differences in the mechanical behavior between the models with multiple unit cells and those with a single unit cell. The interaction between the hard- and soft phases was modeled using surface-to-surface penalty contact with a friction coefficient of 0. A tensile displacement of 10 mm along the longitudinal direction ($U_y = 10$) was applied to the top reference point over a time span of 1 s. The output data, specifically the reaction force, RF_y, and displacement, U_y, of the top reference point, were generated at fixed time increments of 10^{-3} s. Simulations that due to computational limitations (e.g., the absence of rupture mechanics) resulted in unrealistic strains were excluded from the analysis.

Additively Manufactured 2.5D Interfaces: To experimentally test these interface designs and validate the simulation data, 3D printing was employed to realize the soft–hard interface structures. Based on the outcomes of the simulations, two variations of each geometry type were selected for fabrication: AT 45-3-3, AT 60-4-3, DH 6-8-8-7, and DH 4-8-6-6. A schematic representation of these specimens is provided in Figure 1d, illustrating the arrangement of 6 unit cells ($n = 6$), each with a width (w) of 2.88 mm. These specimens were produced with a bulk height (h_b) of 3.5 mm and a thickness of 7 mm. To facilitate the tensile tests, modifications were made to the hard phase of the specimens. Protruding grips, which were designed to interface seamlessly with the matching grip claws attached to the tensile machine, were integrated into the specimen extremities. Additionally, tapered pillars were incorporated that protrude into both hard parts to aid in alignment during the crosslinking and tensile test stages. The tapering of these pillars was specifically engineered to minimize the impact of frictional forces on the measured forces during testing.

Similarly, control specimens were produced to compare the performance of these interfaces (Figure S1, Supporting Information).

The fabrication of the interface models followed a structured series of steps (Figure 1e). First, an FDM 3D printer equipped with a 0.25 mm nozzle (UltiMaker 3, Ultimaker B.V., Netherlands) was used to print the hard phase. The specimens were printed with a layer height of 0.2 mm, a line width of 0.25 mm, a printing speed of 30 mm s^{-1}, 100% infill, 100% fan speed, and nozzle and print bed temperatures maintained at 220 and 60 °C, respectively. The parts were printed with the interface directly on the print bed to eliminate the need for support or post-processing. Subsequently, the soft phase was printed directly atop the hard phase through extrusion-based hydrogel 3D printing using an extrusion-based bioprinter (BioScaffolder 3.2, GeSiM Bio-instruments, Germany). To achieve both interlocking efficiency and structural stability, two distinct pre-crosslinking concentrations of $CaCl_2$ were used for the hydrogel ink. A 1 mM pre-crosslinked hydrogel was used for the infill of the interlocking geometry, facilitating flow into the corners of the geometries during printing. The bulk material was formed using a 15 mM pre-crosslinked hydrogel, ensuring sufficient rigidity to prevent collapse. Both hydrogels were preconditioned for 24 h at 7 °C prior to printing. The interlocking infill was printed using a 0.25 mm nozzle, positioned inside the cavities at 0.58 mm above the interface surface with an extrusion pressure of 20 kPa, aimed at achieving slight over-extrusion at a speed of 100 mm min^{-1}. The bulk was printed using a 0.84 mm nozzle at 25 kPa and a speed of 500 mm min^{-1}. No heating was applied during the printing of the soft phase. The following step consisted of merging two of the soft–hard structures by aligning, stacking, and maintaining them 7 mm apart via the tapered pillars (Figure 1d). The final step consisted of the post-crosslinking of the entire assembly. This was accomplished through submersion in a 200 mM $CaCl_2$ solution for 24 h at 7 °C, effectively merging both soft bulk parts and homogenizing the entire soft phase.

To further validate the computational and experimental models, each interface design was additionally fabricated through Polyjet-printing (Objet350 Connex3 PolyJet 3D printer (Stratasys Ltd., USA)). This method was chosen for its multi-material printing capabilities and higher precision, allowing for more controlled fabrication than when using hydrogels. For this process, two distinct materials were used: VeroCyan (RGD841, Novamatrix) ($E = 0.73$ GPa, $\nu = 0.33$[36]) for the hard phase, and Agilus30 (FLX935, Novamatrix) ($E = 0.60$ MPa, $\nu = 0.45$[36]) for the soft phase. Both phases were printed separately and assembled after removal of their support structures to prevent chemical adhesion. To facilitate an in-depth examination of the strain distribution characteristics of each interface design, these specimens were printed at a larger scale ($125 \times 3 \times 75$ mm^3).

Tensile Tests: Force–displacement data for each specimen was obtained through tensile testing using a mechanical testing machine equipped with a 5 N load cell (LR-5K, Lloyd Instruments Ltd., UK). The testing protocol involved loading the specimens at a rate of 0.02 mm s^{-1} until complete failure, which was defined as the total separation of the phases. Customized tensile test grips (Figure 1d) were used to secure the specimens. These grips were designed with a geometry that matched the protruding grips on the specimens, with a tolerance of 1 mm to prevent any pre-loading. Each specimen design was produced and tested in triplicate. In addition to the force–displacement measurements, strain-distribution data was captured through full-field strain mapping (equivalent von Mises strains) of the Polyjet-printed specimens using a 3D DIC system (Q-400 equipped with two 12 MPixel cameras, LIMESS GmbH, Germany) and its associated software (Instra 4D v4.6, Danted Dynamics A/S, Denmark). The DIC process was conducted at a frequency of 1 Hz. Prior to imaging, the specimens were prepared by painting them white and applying a black dot speckle pattern to facilitate accurate strain mapping. The imaging was performed during tensile testing with a 100 N load cell (LR-5K, Lloyd Instruments Ltd., UK) at a rate of 2 mm min^{-1}.

In the post-processing phase, the tensile test data were first filtered to exclude the initial segment where forces registered below 0.03 N. This step ensured the analysis focused on the significant force-bearing phase of the tests. From the refined force–displacement data, three parameters were derived for evaluating the interface performance: maximum force (F_{max}), stiffness (K), and toughness (W). F_{max} was defined as the maximum measured force while K was calculated using a moving linear regression method with a window size of 15 datapoints, identifying the maximum slope of the force–displacement curve. W was defined as the total area under the force–displacement curve, representing the energy absorption capacity of the interface. To facilitate a meaningful comparison between the computational and experimental results, the computational data was scaled to match the experimental specimen dimensions, according to Equation (1).

$$F_{norm} = \frac{F_{comp} \times n_{exp} \times h_{b,exp}}{h_{b,comp}} \quad (1)$$

Here, the maximum measured force (F_{comp}) is normalized (F_{norm}) relative to the experimental specimen dimensions. The scaling factor considered the number of experimental unit cells (n_{exp}) and the ratio of the experimental to computational bulk heights ($h_{b,exp}$ and $h_{b,comp}$, respectively), ensuring an accurate and direct comparison of the performance metrics.

Statistical Analysis: To assess whether significant differences existed between computationally and experimentally obtained results analyses of variance were performed using one-way ANOVA through IBM SPSS Statistics 29 Software. To determine the significance between the performance of different interface designs, pairwise comparisons were made. The Levene[37] and Shapiro–Wilk[38] tests were performed to test for the homogeneity of variances and normality, respectively, to ensure robustness of results obtained through ANOVA. A p value less than 0.05 was considered statistically significant.

Supporting Information

Supporting Information is available from the Wiley Online Library or from the author.

Acknowledgements

This project was part of the NWO grant OCENW.XS22.2.044 obtained by M.J.M.

Conflict of Interest

The authors declare no conflict of interest.

Data Availability Statement

The data that support the findings of this study are available from the corresponding author upon reasonable request.

Keywords

(Multi-material) 3D printing, hydrogel attachments, mechanical interlocking, soft–hard connections, soft–hard interface design

Received: July 5, 2024
Revised: November 22, 2024
Published online:

[1] Z. Wu, *Int. J. Mech. Sci.* **2008**, *50*, 641.
[2] Y. Gao, X. Jiang, P. Wang, Y. Zhong, T. Lu, *Extr. Mechan. Lett.* **2023**, *61*, 102016.

[3] A. J. Boys, M. C. McCorry, S. Rodeo, L. J. Bonassar, L. A. Estroff, *MRS Commun.* **2017**, *7*, 289.
[4] C. Pitta Kruize, S. Panahkhahi, N. E. Putra, P. Diaz-Payno, G. van Osch, A. A. Zadpoor, M. J. Mirzaali, *ACS Biomater. Sci. Eng.* **2023**, *9*, 3810.
[5] L. M. Galatz, L. J. Sandell, S. Y. Rothermich, R. Das, A. Mastny, N. Havlioglu, M. J. Silva, S. Thomopoulos, *J. Orthopaed. Res.* **2006**, *24*, 541.
[6] K. E. M. Benders, P. R. V. Weeren, S. F. Badylak, D. B. F. Saris, W. J. A. Dhert, J. Malda, *Trends Biotechnol.* **2013**, *31*, 169.
[7] A. Dimaraki, P. J. Díaz-Payno, M. Minneboo, M. Nouri-Goushki, M. Hosseini, N. Kops, R. Narcisi, M. J. Mirzaali, G. J. V. M. van Osch, L. E. Fratila-Apachitei, A. A. Zadpoor, *Appl. Sci.* **2021**, *11*, 7821.
[8] Y. Li, M. Zhou, W. Zheng, J. Yang, N. Jiang, *Regen. Biomater.* **2023**, *10*, rbac091.
[9] H. Zhang, Y. Ma, Y. Wang, L. Niu, R. Zou, M. Zhang, H. Liu, G. M. Genin, A. Li, F. Xu, *Small* **2023**, *19*, 2204498.
[10] R. C. Nordberg, D. H. Wen, D. Wang, J. C. Hu, K. A. Athanasiou, *Curr. Opin. Biomed. Eng.* **2024**, *31*, 100546.
[11] E. Pesare, R. Vitiello, T. Greco, G. Solarino, G. Maccauro, A. Ziranu, *Curr. Oncol.* **2024**, *31*, 7190.
[12] J. Chen, J. Xu, A. Wang, M. Zheng, *Expert Rev. Med. Devices* **2009**, *6*, 61.
[13] D. Bicho, S. Pina, R. L. Reis, J. M. Oliveira, in *Osteochondral Tissue Engineering*, Springer International Publishing, Berlin/New York **2018**, pp. 415–428.
[14] W. Wang, Y. Sun, Y. Lu, J. Wang, Y. Cao, C. Zhang, *J. Mech. Behav. Biomed. Mater.* **2021**, *113*, 104137.
[15] M. C. Saldívar, E. Tay, A. Isaakidou, V. Moosabeiki, L. E. Fratila-Apachitei, E. L. Doubrovski, M. J. Mirzaali, A. A. Zadpoor, *Nat. Commun.* **2023**, *14*, 7919.
[16] M. C. Saldívar, E. L. Doubrovski, M. J. Mirzaali, A. A. Zadpoor, *Addit. Manuf.* **2022**, *58*, 103062.
[17] M. C. Saldívar, S. Salehi, R. P. Elias Veeger, E. Tay, M. Fenu, A. Cantamessa, M. Klimopoulou, G. Talò, M. Moretti, S. Lopa, D. Ruffoni, G. J. V. M. van Osch, L. E. Fratila-Apachitei, Z. Doubrovski, M. J. Mirzaali, A. A. Zadpoor, *Cell Rep. Phys. Sci.* **2023**, *4*, 101552.
[18] T. Kuipers, R. Su, J. Wu, C. C. L. Wang, *Addit. Manuf.* **2022**, *50*, 102495.
[19] O. E. Armitage, M. L. Oyen, in *Engineering Mineralized and Load Bearing Tissues*, Springer International Publishing, Berlin/New York **2015**, pp. 187–204.
[20] I. Calejo, R. Costa-Almeida, R. L. Reis, M. E. Gomes, *Trends Biotechnol.* **2020**, *38*, 83.
[21] R. Balokhonov, V. Romanova, *Facta Uni., Series: Mechan. Eng.* **2019**, *17*, 169.
[22] J. H. Waite, H. C. Lichtenegger, G. D. Stucky, P. Hansma, *Biochemistry* **2004**, *43*, 7653.
[23] S. Thomopoulos, V. Birman, G. M. Genin, *Structural Interfaces and Attachments in Biology*, Springer, Berlin/New York **2013**.
[24] R. T. Rao, D. P. Browe, C. J. Lowe, J. W. Freeman, *Connect. Tissue Res.* **2016**, *57*, 53.
[25] O. E. Armitage, M. L. Oyen, *Acta Biomater.* **2017**, *56*, 36.
[26] L. Rossetti, L. A. Kuntz, E. Kunold, J. Schock, K. W. Müller, H. Grabmayr, J. Stolberg-Stolberg, F. Pfeiffer, S. A. Sieber, R. Burgkart, A. R. Bausch, *Nat. Mater.* **2017**, *16*, 664.
[27] E. Lin, Y. Li, C. Ortiz, M. C. Boyce, *J. Mech. Phys. Solids* **2014**, *73*, 166.
[28] Z. Wu, *Eng. Fract. Mech.* **2006**, *73*, 953.
[29] D. M. Kirchmajer, R. Gorkin Iii, M. In Het Panhuis, *J. Mater. Chem. B* **2015**, *3*, 4105.
[30] L. Zhou, P. Guo, M. D'Este, W. Tong, J. Xu, H. Yao, M. J. Stoddart, G. J. V. M. van Osch, K. K.-W. Ho, Z. Li, L. Qin, *Engineering* **2022**, *13*, 71.
[31] L. M. Cross, A. Thakur, N. A. Jalili, M. Detamore, A. K. Gaharwar, *Acta Biomater.* **2016**, *42*, 2.
[32] M. J. Mirzaali, V. Moosabeiki, S. M. Rajaai, J. Zhou, A. A. Zadpoor, *Materials* **2022**, *15*, 5457.
[33] Y. Zhang, H. Yao, C. Ortiz, J. Xu, M. Dao, *J. Mech. Behav. Biomed. Mater.* **2012**, *15*, 70.
[34] J. Torres, J. Cotelo, J. Karl, A. P. Gordon, *JOM* **2015**, *67*, 1183.
[35] The Definitive Guide to ASTM D412 Tensile Testing of Elastomers, https://www.instron.com/en/testing-solutions/astm-standards/astm-d412 (accessed: May 2023).
[36] M. J. Mirzaali, A. Herranz de la Nava, D. Gunashekar, M. Nouri-Goushki, R. P. E. Veeger, Q. Grossman, L. Angeloni, M. K. Ghatkesar, L. E. Fratila-Apachitei, D. Ruffoni, E. L. Doubrovski, A. A. Zadpoor, *Compos. Struct.* **2020**, *237*, 111867.
[37] B. Mandelbrot, *SIAM Rev.* **1961**, *3*, 80.
[38] S. S. Shapiro, M. B. Wilk, *Biometrika* **1965**, *52*, 591.